Eng. Sci., 2022, **19**, 100–113

Engineered Science
DOI: https://dx.doi.org/10.30919/es8d642

Characterization of Wicking Performance for Open Rectangular Microgrooves under Planar Electrohydrodynamics Effects in Two-phase Heat Transfer Devices

Jinchen Tang, Zhe Chen, Yu Ma and Hang Zhang*

Abstract

Advanced thermal management for future electronics has promoted the development and investigation of two-phase heat transfer devices (*i.e.*, micro heat pipes, vapor chambers, capillary pumped loops, *etc.*). Electrohydrodynamics (EHD) pumping is an attractive solution to insufficient liquid supply and dry-out occurrence in the wicks of such devices. In this study, the wicking performance of rectangular microgrooves is characterized and evaluated by an axial maximum capillary wetting length at a steady state and dynamic rise rate at a transient state during rate-of-rise experiments. Two planar electrodes are used to generate an electric field. The maximum axial capillary wetting length under EHD effects at steady state is experimentally conducted and theoretically analyzed, and the predicted results agree well with the experimental data. The dynamic wicking characteristics considering the electric field are investigated at the transient state, and the empirical correlations are obtained according to the fitting experimental data as $h^2 \sim t$ curve at the initial stage, and $\frac{h}{t} \sim k e^{-\frac{t}{\tau}}$ curve at the long-term stage. The EHD pumping mechanism is also analyzed. EHD effects can decrease the wall temperature of microgrooves. There exists an optimal electric voltage to obtain the highest economic efficiency and wicking performance in this study.

Keywords: Electrohydrodynamics (EHD); Two-phase heat transfer device; Wicking performance; Steady state; Transient state.
Received: 24 December 2021; Revised: 29 January 2022; Accepted: 31 January 2021.
Article type: Research article.

1. Introduction

Micro heat pipes, vapor chambers, and capillary pumped loops are well-known simple and effective two-phase heat transfer devices,[1,2] that use capillary pressure flow and phase change heat transfer to dissipate heat. It has great application prospects in energy conversion and thermal management of high-power electronic devices and microelectronic equipment cooling.[3] However, the generation of capillary pressure requires capillary structures, such as porous materials or porous structures in the required flow direction, and the total heat transfer capacity of which is usually limited by the amount of capillary pressure generated by capillary structures.[4–6]

Among the structures of those two-phase heat transfer devices, the open microgrooves wicks are particularly attractive because of two orders of magnitude higher liquid permeability compared with the conventional sintered porous wicks,[5,7] which results in small viscous friction at high heat flux.[8,9] As shown in Fig. 1, when the microgrooves wick is located vertically or inclined in a liquid pool, the liquid in open microgrooves is driven by the capillary force and disjoining pressure generated by its geometric structure, and forms an extended meniscus upward along the axial direction of microgrooves.[10,11] However, at a relatively high heat flux, the wetting liquid would gradually dry out down along the microgrooves, which could result in the low efficiency and instability of the two-phase heat transfer device.

Electrohydrodynamic (EHD) effects have been significantly proven to enhance the wicking capability and heat transfer characteristics. For instance, Tang *et al.*[4,12,13] used pin-plate electrodes pair to control the wetting flow of the liquid film in the open microgrooves, and found that the liquid film increased greatly in the local area of the microgrooves. Results show that the capillary wetting length increases with the increasing electric field intensity, and the

Institute of Engineering Thermophysics, Chinese Academy of Sciences, Beijing 100190, China.
**E-mail:* zhanghang@iet.cn (H. Zhang)

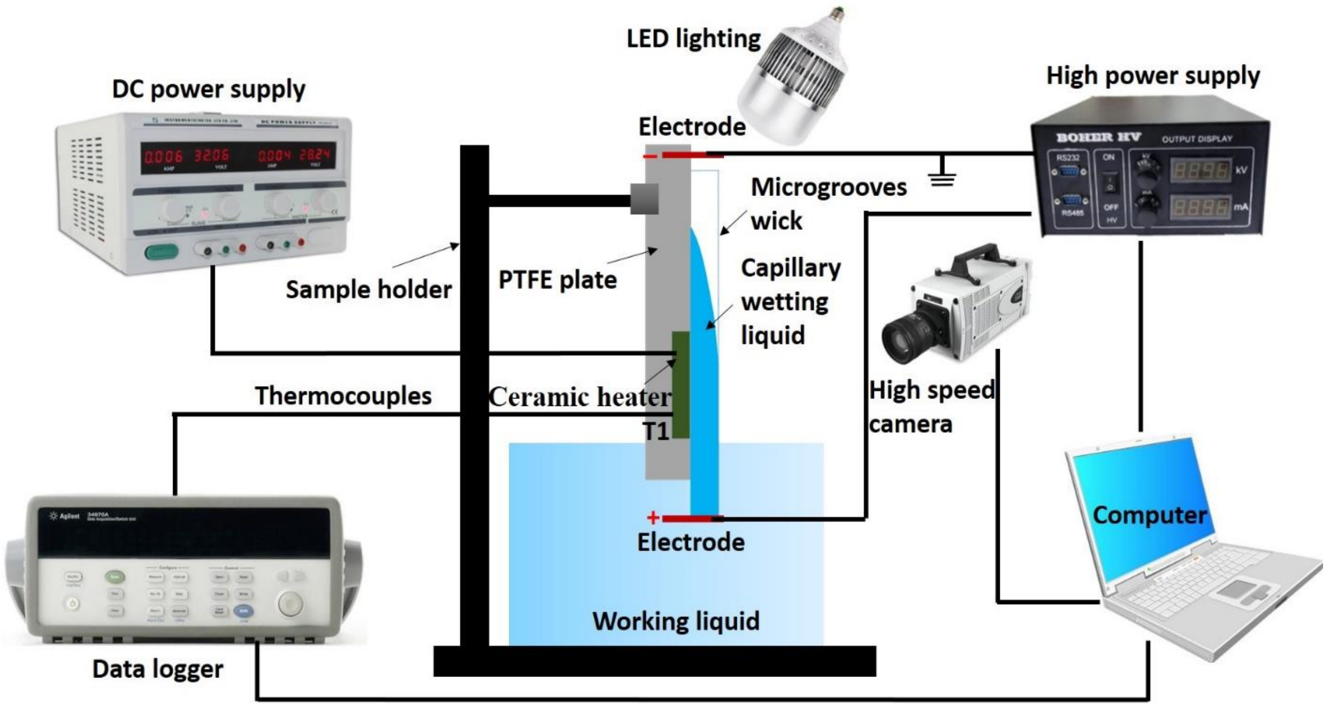

Fig. 1 Schematic of experimental apparatus.

microgrooves wall temperature decreases with the increasing electric field intensity. Yu *et al*.[14] studied the heat transport capability of EHD augmented micro heat pipes by conducting experiments, which indicates that the heat transport capability of the EHD micro heat pipes was increased by up to six times than that of conventional ones. Migliaccio *et al*.[15] applied electric field to study the evaporation of liquid droplets on a heated surface, and found that EHD effects can increase the equilibrium wetting area of liquid to 170%, which makes the liquid drop has a higher evaporation rate (increased by about 57%). Bahadur *et al*.[16] studied different technologies based on EHD effects in microelectronic thermal management: one is to control the movement of liquid droplets on the chip surface by an electric field, and then cool the heating chip; The other is to control the shape of droplets on the surface by an electric field, to realize the thermal management of heat source.

As one of the inspiring structures for two-phase heat transfer devices, the wicking ability of open microgrooves is limited by the capillary pressure, which affects the heat transfer performance of the two-phase heat transfer devices.[17–20] However, when the heat flux becomes higher, the evaporation thin liquid film may dry out, resulting in the deterioration of the phase change heat transfer of the two-phase heat transfer devices. To maintain the stability of the highly intense phase change heat transfer capability of the devices, it is necessary to replenish the capillary wetting liquid to the dried area, insuring continuous high-intensity phase change heat transfer.[21–23] Because the high-intensity evaporation or boiling of the wetting liquid film in the open microgrooves is mainly concentrated on the extended meniscus near the three-phase contact line,[24] the electrowetting tension in the EHD effect is acting on the three-phase contact line of the liquid film. Furthermore, it is proven that the electric field can reduce the contact angle between the liquid film and the heating wall surface.[25] Therefore, we can say that the EHD effects can increase the wetting area of the liquid film, strengthen the wetting ability of the liquid film, and facilitate the high-intensity evaporation or boiling of the liquid film.

In this paper, we develop a planar electrodes pair, namely plate-plate electrodes, to produce the electric field, and study the EHD effects on the rectangular microgrooves (RMs). The wicking performance of RMs is characterized and evaluated by the axial maximum capillary wetting length at steady state and the dynamic rise rate at transient state during rate-of-rise experiments, which is important to know but not referred to in previous studies. Especially, the capillary wetting length is defined as the length from the level of the liquid pool to the dry-out point,[6,12] which is characterized by the capillary force of microgrooves,[4,12,26,27] together with affecting the amount of liquid in microgrooves, intensive evaporating area of the thin liquid film, and critical heat flux in microgrooves.[3,10,25] In addition, the dynamic rise rate can evaluate the flow rate of liquid replenished from the liquid reservoir to the dried area of microgrooves in time. Thus, the axial capillary wetting length and the dynamic rise rate of microgrooves play a key role in determining the thermal performance as well as understanding the heat transfer mechanism, and further developing the advanced thermal strategies for the wick structures of microgrooves.[4,9,12,26,27] Furthermore, theoretical analysis on the axial capillary wetting length and the rising rate in the RMs are also performed to promote the understanding of the axial capillary flow characteristics. The calculation results agree well with the experimental data.

2. Experimental system

2.1 Experimental apparatus

Figure 1 illustrates the schematic of the experimental apparatus and measured layout in the experimental applications, which is similar to that in our previous studies.[4,12] It is mainly composed of microgrooves experimental components, high-voltage generator, data acquisition system and lighting component. The RMs samples were fabricated with dimensions of 90 mm × 20 mm × 1 mm using precision milling techniques by CapitalBio Co., and the dimensions are shown in Table 1. As shown in Fig. 1, we can see that the RMs heat sink was held by a sample holder. A liquid reservoir made of quartz glass was directly open to the ambient condition, which can ensure that the experiments were performed under atmospheric pressure. A direct current (DC) power supply was used to provide heat to the RMs sample. A ceramic heater (20 mm × 20 mm × 1.7 mm) as the heating element was adhered tightly to the back of the RMs to conduct heat flux. High performance heat conduction silicate grease, with thermal conductivity of 6 W $(m{\cdot}K)^{-1}$ was used between the microgrooves and ceramic heater to minimize the thermal resistance. A PTFE (Polytetrafluoroethylene) thermal insulation cover plate is adhered over the backside of microgrooves and the heating element to reinforce them and reduce the heat loss. A high-power supply (BOHER 73030PA) was utilized to generate electric field. A planar electrodes pair was configured to produce the electric field. The high voltage electrode (immersed in the liquid reservoir of the lower position one in Fig. 1) termed as emitter electrode was connected to the high power supply, while the grounded electrode was placed at the top of the grooves. The enlarged part of electrodes pair of the electrode pair viewed from the y-z plane is shown in Fig. 2. The applied high voltage can be adjusted from 0 kV to 30 kV continuously, and the corresponding current could be read from the high-power supply simultaneously. The maximum output current (1 mA) is far below the safe current level for human contact. The data acquisition system includes the computer, data logger, high-speed camera. Agilent (34970A) connecting thermocouples is used as the data logger to record the temperatures of the back of the RMs with EHD effects. A K-type armored thermocouple connected the data logger was inserted a preserved hole located between the ceramic heater and PTFE plate with heat conduction silicate grease to determine the temperature (T) of RMs wick sample under EHD effects. A light emitting diode (LED) lighting device, which was used for capturing the axial wetting length in microgrooves. High-speed camera was used to visualize and measure the wetting length. Distilled water was selected as the working fluid in this study due to its safe, good stability, cheapness, easy to be obtained and widely applied in industries, which is also motivated by other previous studies[28,29] under electric field conditions.

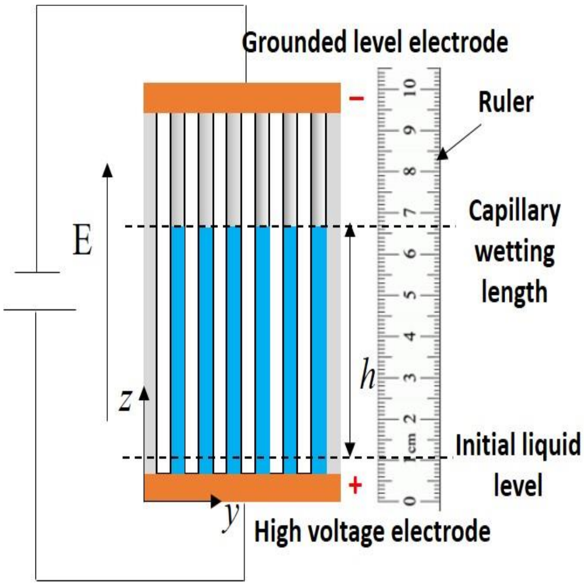

Fig. 2 Electrodes configuration of EHD pumping with planar electrodes pair on the microgrooves for the y-z plane.

Table 1. The actual dimensions of rectangular microgrooves (RMs) for different wick samples by an optical microscope.

Number	The actual dimensions of microgrooves		
	Width w_g (mm)	Depth d_g (mm)	Pitch s_g (mm)
No.1	0.23	0.45	0.44
No.2	0.23	0.55	0.44
No.3	0.23	0.65	0.44
No.4	0.35	0.55	0.44
No.5	0.35	0.65	0.44

2.2 Experimental procedures

Prior to each experiment, the RMs wick sample was washed in an ultrasonic cleaner with detergent, then washed with distilled water, and dried at last, so that the oil and impurity inside the RMs could be cleaned thoroughly. Subsequently, the RMs were vertically or inclined placed in the liquid reservoir with the PTFE plate fixed on the holder. The inclination angle of the sample (inclined at an angle β to the horizontal) can be regulated by the fixture of the PTFE plate in the sample holder. Once the preparatory works were done, the capillary rate-of-rise experiment was conducted in such an open system shown in Fig. 1. The RMs wick was dipped vertically into the liquid reservoir, and the liquid spontaneously rise along the RMs wick due to the capillary pressure. The liquid level of the reservoir is thought to be constant during the capillary rise process due to the very small amount of absorbing liquid in the wicks. Meanwhile, the input power is low, ranging from 0 to 5 W, only evaporation is considered in this study. The rate-of-rise process and the equilibrium axial wetting lengths of liquid in microgrooves were recorded and extracted through the high-speed images recorded by the high speed camera in combination with the adjacent ruler. Thus the capillary rise height over time can be obtained, and the capillary rise time for each test run is recorded as 40 s. For the basic case of without EHD, the rate-of-rise process and equilibrium axial wetting lengths at steady state curve was measured by repeatedly incrementing the prescribed inclination angles, applied heat flux, and recorded the rate-of-rise process and microgrooves wall temperature (T) at each set-point once the steady state was reached. The procedure was repeated when the EHD was applied.

2.3 Data reduction and uncertainty analysis

The detailed uncertainty of each measurement is listed in Table 2. When $R(x)$ is a function of several independent variables x_1, x_2, … x_N, the uncertainty of R is given by the following Table 2[30]:

Table 2. Uncertainties of instruments and properties.

Name	Range	Experimental range	Accuracy	Maximum uncertainty (%)
Applied voltage (U_e)	0–30 kV	0–8 kV	0.01 kV	1.25
Corona Current (I_e)	0–1000 μA	0-75 μA	1 μA	1.3
Heating voltage (V_h)	0–60 V	2-4.2 V	0.01 V	0.5
Heating current (I_h)	0–5 A	0.6-1.6 A	0.01 A	1.67
Thermocouple (T)	-40–125 °C	20-65 °C	0.2 °C	1
Wetting length (h)	0–90 mm	22-60 mm	0.16 mm	0.73

3. Theory

During the capillary rate-of-rise experiments, once the RMs wick contacts the working fluid, a rise of working liquid in the RMs occurs. The electrodes configuration is shown in Fig. 2, and the action of an electric field is generated by the planar electrodes pair. The capillary pressure generated by the liquid-vapor interface considering the EHD effects plays the driving force to pump the liquid flow in the microgrooves.

The description of the liquid rise over time by mathematical methods and its prediction are of great interest, which can be seen in this section. When the liquid is brought into contact with a vertical, or inclined microgrooves, it spontaneously rises up to a final height h_{max}. The rising liquid flows fast at first and slows down later, until reaches a steady state finally.[6,31–33] The following assumptions hold in the present study[27,34]: (1) one-dimensional flow along the microgrooves; (2) the heat transfer conducted through the microgrooves wall is neglected. (3) The vapor pressure is constant since the experimental setup is in an open system. (4) The bubble flow is not considered since only evaporation with low heat flux is taken into account.

The mechanism governing the EHD phenomenon requires an analysis of forces acting on a dielectric fluid. The equation of electric force per unit volume is widely expressed as,[35]

$$F_e = q_e E_l - \frac{1}{2} E_l^2 \nabla\varepsilon + \frac{1}{2} \nabla\varepsilon [E_l^2 \left(\frac{\partial\varepsilon}{\partial\rho}\right)_T \rho \qquad (1)$$

where q_e is the volume of electric charge density. ε and ρ are the fluid permittivity and the fluid density, respectively. The three terms on the right-hand side of Eq. (1) represent the Coulomb force, the dielectrophoretic force, and the electrostrictive force, which is due to the non-uniformity of the electric field in the dielectric medium in this study, respectively.

With these assumptions the forces balance of the RMs in the liquid can be given:

$$F_c + F_e = F_{l,f} + F_g \qquad (2)$$

where F_e and F_c is EHD force and capillary forces, respectively. $F_{l,f}$ is liquid-wall shear stress. F_g is the gravity component. Hence, the working fluid pumped by EHD force along the microgrooves works properly if the capillary forces F_c and the EHD forces F_e are able to overcome the pressure losses $F_{l,f}$.

The liquid-vapor interface equilibrium can be written as the Laplace-Young equation,

$$F_c + F_e = \frac{dP_l}{dz} \qquad (3)$$

The arrangement of the electrodes in Fig. 2, is referred to as "horizontal electrodes". In this case, by neglecting the electric field distortion caused by the liquid-vapor interface, the dielectric constant with density varies little, and the electrostrictive force can be ignored. Only coulomb force and dielectric force are considered to pump the liquid.[36] Hence, the liquid-vapor interface equilibrium with a modified Young-Laplace equation is written as [37,38]

$$F_c + F_e = \frac{\sigma_l}{r_c(z)} + q_e E_l + \frac{1}{2} E_l^2 (\varepsilon_l - \varepsilon_v) \qquad (4)$$

Here, $r_c(z)$ is the equivalent meniscus radius of curvature of the liquid, σ_l is the surface tension of the liquid. ε_l and ε_v is the dielectric constant of liquid and vapor, respectively. E_l is the electric field intensity in the liquid phase. It is given by the Crowly formula[4,37] as follows:

$$E_l = \frac{V}{d_e} [\left(1 - \frac{e(r_c)}{d_e}\right) \frac{\varepsilon_l}{\varepsilon_v} + \frac{e(r_c)}{d_e}]^{-1} \qquad (5)$$

V is the applied voltage, d_e is the depth of the groove, and $e(r_c)$ is a function of the radius of curvature $r_c(z)$ and contact angle θ that can be expressed as [4,36]

$$e(r_c) = [\frac{\cos\left(\theta + \frac{\pi}{4}\right)}{\tan\left(\frac{\pi}{4}\right)} + sin\left(\theta + \frac{\pi}{4}\right) - 1] r_c(z) \qquad (6)$$

The gravity component F_g is expressed as:

$$F_g = \rho_l g sin\beta \qquad (7)$$

where β is the inclined angle to the horizontal plane, ρ_l is the liquid density.

The term of liquid-wall shear stress $F_{l,f}$ can be treated as 2 ways: For the capillary rise process at transient state, it relates to the dynamic wicking characteristics with a function of rising time. While for the capillary wetting at steady state, it presents the maximum wetting length that the microgroove can reach.

Based on the assumption of Poiseuille flow, the viscous friction force ($F_{l,f}$) can be obtained as follows,[6,7,39]

$$F_{l,f} = 8\pi\mu z\frac{dz}{dt} \tag{8}$$

By integration of Eqs. (4, 7-8) into Eq. (2), the following can be obtained as,

$$\frac{\sigma_l}{r_c(z)} + q_e E_l + \frac{1}{2}E_l^2(\varepsilon_l - \varepsilon_v) = \frac{8\mu z dz}{z^2 dt} + \rho_l g sin\beta \tag{9}$$

where μ is the viscosity of liquid, z is the capillary rise length in grooves with the time. The whole capillary rise process is governed by Eq. (9), whereas different flow dynamics may exist. In this study, we will discuss the EHD effects on the axial capillary wetting length at steady state and transient state respectively in section 4 in detail.

The rising liquid flows fast at first and slows down later, while for a longer time, when the liquid reaches at steady state, the axial capillary wetting length reaches its maximum, and it does not vary with time. In that case, the liquid-wall shear stress $F_{l,f}$ can be derived from Darcy Weisback equation from open microgrooves is expressed as follows[8,11]:

$$F_{l,f} = \frac{2Po_l \dot{m} v_l}{A_c D_h^2} \tag{10}$$

Here $\dot{m}$ and v_l are mass flow rate and kinematic viscosity of liquid, respectively. A_c is the cross-sectional area of liquid in the microgrooves. While D_h is the corresponding hydraulic diameter, which can be expressed by A_c and the wetted perimeter P_h of the liquid in the cross section of microgroove: $D_h = 4A_c/P_h$. Po_l is the Poiseuille number of liquid flow.

The Poiseuille number Po_l, depends on the microgroove geometry,[27,40]

$$\mathrm{Po}_l = 32d_g^2\left[w_g^2\left(1+\frac{2d_g}{w_g}\right)^2\left(\frac{1}{3}-\frac{32w_g}{\pi^5 d_g \tanh\left(\frac{\pi d_g}{w_g}\right)}\right)\right]^{-1} \tag{11}$$

The heat flux is assumed to be uniformly applied to the underside of the groove, therefore, the axial mass flow rate at any z-position can be expressed as[4,8]

$$\dot{m} = \frac{w_g+s_g}{h_{fg}}\int_z^{h_{max}} q(z)dz \tag{12}$$

Here w_g, s_g are the width and pitch of grooves, $q(z)$ is the heat flux and h_{fg} is the liquid latent heat of evaporation. As a result, Eq. (2) can be further presented as:

$$\frac{\sigma_l}{r_c(z)} + q_e E_l + \frac{1}{2}E_l^2(\varepsilon_l - \varepsilon_v) = \frac{2Po_l \dot{m} v_l}{A_c D_l^2} + \rho_l g sin\beta \tag{13}$$

Based on the accommodation theory illustrating fundamental features of the axial flow in an open microgroove structure partially dipped in a liquid reservoir,[8,18,41] the capillary flow can be divided into two regions, *i.e.*, accommodation flow region and triangular corner flow region.[8] As shown in Fig. 2, the accommodation flow region (Figs. 3(a)-(c)) Z_a refers to the region starting from the flow entry of the groove in Fig. 3(a), where the liquid completely fills the grooves and the air-liquid interface is flat, and terminating at the fully conformed position in Fig. 3(c), where the liquid film completely accommodates the microgroove geometry and the height of the centerline film. While the triangular corner flow region Z_t indicates that the liquid flows in two identical triangular sections until it dries out in Fig. 3(d).

In the accommodation flow region ($0 \le z \le h_a$), the geometric conditions are given as,

$$A_{l,a} = w_g h_{lw} - (\varphi r_c^2 - \frac{1}{2}r_c^2 sin2\varphi) \tag{14}$$

$$P_{lw,a} = w_g + 2h_{lw} \tag{15}$$

and the boundary conditions are as follows,

$$z = 0,\ r_c(z) = \infty \tag{16}$$

$$z = h_a,\ r_c(z) = \frac{w_g}{2cos\theta} \tag{17}$$

h_c, h_{lw} are auxiliary drawing distances, which can be seen in Fig. 3, here φ is equal to $\pi/2-\theta$, and $A_{l,a}$ $P_{lw,a}$ is the wetting cross-sectional area and perimeter of the liquid-wall interface.

In the triangular corner flow region ($0 \le z \le h_{max}$), the geometric conditions are given as,

$$A_{l,t} = 2(sin^2\varphi - \varphi + 0.5sin2\varphi)r_c^2 \tag{18}$$

$$P_{lw,t} = \frac{4r_c sin\varphi}{cos\frac{\pi}{4}} \tag{19}$$

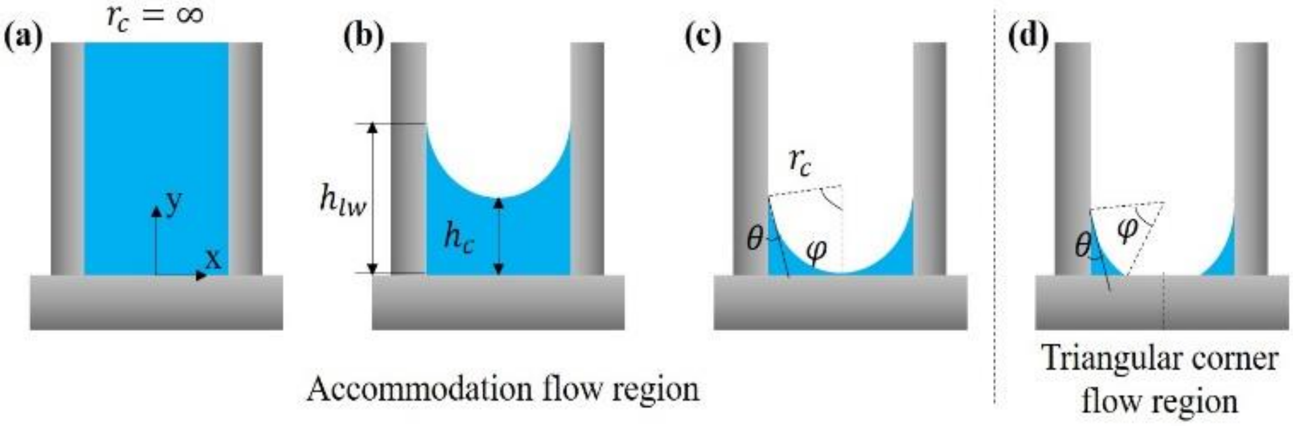

Fig. 3 Liquid flow configuration in the cross-section of microgroove.

and the boundary conditions are given as,

$$z = h_a,\ r_c(z) = \frac{w_g}{2cos\theta} \tag{20}$$

$$z = h_{max},\ r_c(z) = r_{min} \tag{21}$$

Here, half of the apex angle φ is $\pi/4-\theta$. The liquid hydraulic diameter D_l equals to $4A_l/P_{lw}$. r_{min} is determined by the manufacturing method used to produce the microgrooves, and 100 μm is selected here in this study due to precision milling techniques.[8,27] From the iterative calculation of Eq. (13) by combining geometric conditions and boundary conditions of Eqs. (14-21) in the accommodation flow region and triangular corner flow region, the total capillary wetting length in these two regions along the axial direction can be obtained by the Runge-Kutta method of order 4.

4. Results and discussion

4.1 EHD effects on the axial capillary wetting length at steady state

When the liquid is brought into contact with vertical, or inclined microgrooves, it spontaneously rises up to a final length h_{max}. The rising liquid flows fast at first and slows down later, until reaches at a steady state finally.[6] So the capillary wetting length is defined as the length from the initial level of liquid to the dryout point along the axial direction of microgrooves, which is one of the key parameters to evaluate the wicking performance of microgrooves wick. It determines the dryout of capillary rise limit and heat transfer performance that may usually encounter in the situations of high heat fluxes. It is critical to evaluate this performance to ensure the good design and thermal management of the microgrooves.

The capillary wetting lengths under different electric field voltages at steady state were experimentally investigated. Fig. 4 illustrates the experimental results of capillary wetting length as a function with different inclined angles under different electric voltages for No. 1 and No. 4 microgrooves. It is noted to see that the wetting length decreases with the increased inclined angles. When the inclination angle of the microgrooves is small, that is, in the horizontal situation, it is obvious to see the greater importance of electric field force than that in the vertical situation. When the inclined angle is 30°, the wetting length in the microgrooves under the action of electric field increases by 38.4% compared to without an electric field (0 kV), and the increasing rate is more than 6 times which under vertical conditions. The reason is that with the increase of the inclination angle, the force of the electric field on the fluid remains unchanged, while the component of gravity along the axial microgrooves gradually strengthens, so the relative importance of the electric field, compared with the gravity component, to the wetting enhancement in the microgrooves is weakened.

When the microgroove is subject to an input heat flux, a large amount of liquid is lost due to evaporation heat transfer, resulting in stable axial supplementary flow, which produces viscous friction on the microgrooves wall opposite the flow direction. The visualized capillary wetting length experimental results under the electric field (in the range of 0-8 kV) at different heat flux (in the range of 2-4.5 kW m^{-2}) for No. 1 microgrooves are illustrated in Fig. 5. At this time, the electrode distance between the positive electrode and the negative electrode is 55 mm. It is found that the electric field enhances to a greater extent at the smaller heat flux. When the heat flux is 2 kW m^{-2}, the capillary wetting length is 23.2mm without an electric field; while the electric voltage increases to 7.5 kV, the liquid in the microgrooves is driven by the electric field flows upward along it, and the maximum capillary wetting length reaches 52.4 mm, with a growth rate of 125.9%. However, it is found that the wetting length gradually decreases with the increase of input heat flux. According to Darcy Weisbach's equation $F_{l,f} = \frac{2Po_l\dot{m}v_l}{A_cD_l^2}$ (Eq. (10)), the mass flow rate $\dot{m}$ is directly proportional to the heat flux (Eq. (12)),[11,42] so the flow resistance is directly proportional to the heat flux. Therefore, with the increase of heat flux, the fluid flow resistance increases, correspondingly, the ability to enhance the wetting liquid in the microgrooves decreases.[43] It is found that there is an optimal strengthening voltage, which corresponds to the maximum wetting length that can be achieved in the microgrooves, which has a similar trend as Yu's research.[43]

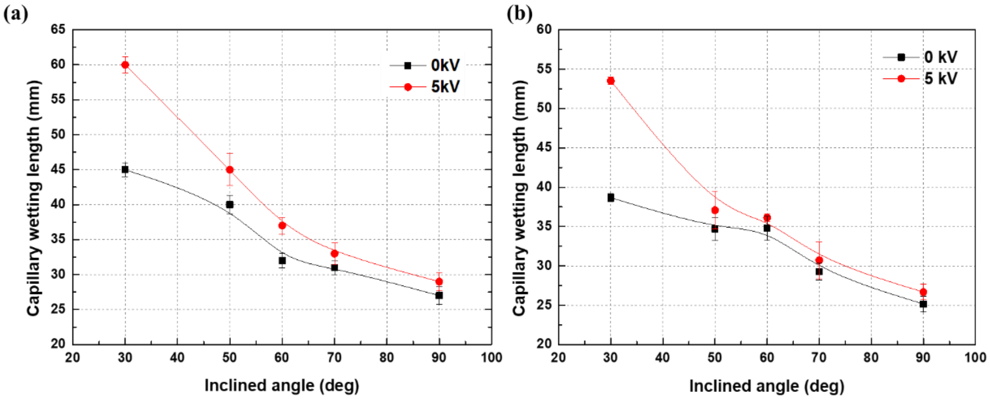

Fig. 4 The experimental data of the relationships between axial capillary wetting length and inclined angle for (a) No. 1 RMs and (b) No. 4 RMs with different applied electrical voltages of 0 kV and 5 kV under unheated conditions.

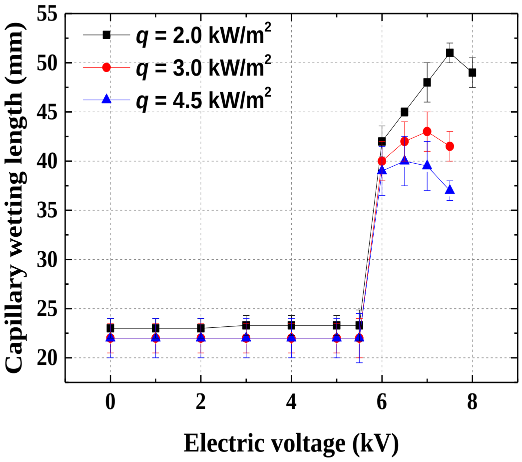

Fig. 5 The experimental data of the relationships between axial capillary wetting length and applied electric voltages(in the range of 0-8 kV) for No. 1 RMs with different applied input heat fluxes (in the range of 2-4.5 kW m^{-2}) under heated conditions.

The maximum axial capillary wetting length are also predicted and analyzed by the theoretical model at steady state proposed in the theory part in section 3, in order to understand the EHD effects on the capillary wetting length at steady state. As Eq. (2) descripts, when there is no electric field applied, the liquid in the microgrooves is driven by capillary force to overcome the resistance and gravity and climb along the axial direction of the RMs. While the electric field is applied, besides the driving action of capillary force, the electric field force also becomes the force driving the liquid to climb force also becomes the force driving the liquid to climb along the microgrooves. The comparisons of wetting length between the theoretical values and experimental data of No. 3 RMs at a heat flux of 2 kW m^{-2} at vertical situation are presented in Fig. 6 and Table 3. It is calculated that the maximum error is 9.2% at the voltage of 5.7 kV, while the error 8.9% at the voltage of 5.6 kV. The predicted results agrees well with the experimental data. The error between them is mainly due to the underestimated calculated results based on the previous assumptions in the theoretical model.

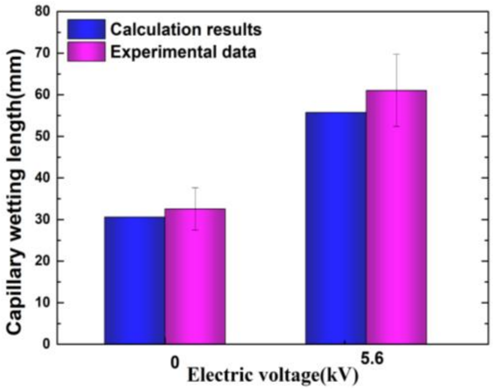

Fig. 6 The experimental data and calculation results of axial capillary wetting lengths for vertical No. 3 RMs samples with 2 kW/m^2 input heat flux under different applied electric voltages (0 kV and 5.6 kV).

Table 3. The calculation results are based on the proposed theoretical model by different applied electric voltages and the measured axial wetting lengths for vertical RMs samples under 2 kW m^{-2} heating conditions.

	Applied electric voltages			
	0 kV	5.5 kV	5.6 kV	5.7 kV
Experimental data h_{max} (mm)	32.5±3.5	61.0±4.2	61.6±4.0	61.8±3.8
Calculation results h_{max} (mm)	30.55	55.70	56.09	56.1

4.2 EHD effects on the dynamic wicking characteristics at transient state

When the liquid is brought into contact with vertical, or inclined open microgrooves, it spontaneously rises up a transient state. Fig. 7 shows the capillary rate-of-rise processes under 3 types of electric voltages. It can be seen that the successive flow of the liquid in the axial microgrooves at the transient state reaches the maximum equilibrium capillary wetting length at a steady state finally. For the same microgrooves under different electric field actions, larger electric voltage provides better capillary pressure to sustain the capillary rise process for the long-term time. Fig. 7(a) shows the variations of capillary wetting length h in a vertical situation during the 40s in the presence of the electric field and in the absence of the electric field. It can be seen from the figure that the capillary wetting length increases exponentially with time regardless of the electric field. It increases sharply in the first 5s and increases slowly in the last 5s-40s. As expected, the microgrooves under a larger electric field exhibit much quicker capillary rise characteristics than that under less electric field action or without it. However, we can find that the electric field has little effect on the wetting length at the initial stage of the rise-of-rate process, with time passing by, the influence of the electric field on wetting length is gradually obvious. The reason for this phenomenon is related to the arrangement of the electrode pair shown in Fig. 2. The parallel planar electrodes pair is utilized to generate the electric field, and the dielectric constant of deionized water is relatively high at $78.4\varepsilon_0$. Here, the distance between the highest point of the wetting length of liquid and the negative electrode can be regarded as the "real electrode spacing". When the wetting length is small, the electrode spacing is large and the electric field intensity is small, resulting in less influence of the electric field. With the increase of time, the liquid gradually climbs along the microgrooves, and the wetting length gradually increases, which is equivalent to the decreasing electrode spacing. It makes the electric field strength gradually increases, and thus the influence of the electric field increases. In order to see the influence of different electric voltages on the capillary wetting length, the time needed to reach the capillary wetting length of 36 mm under different electric

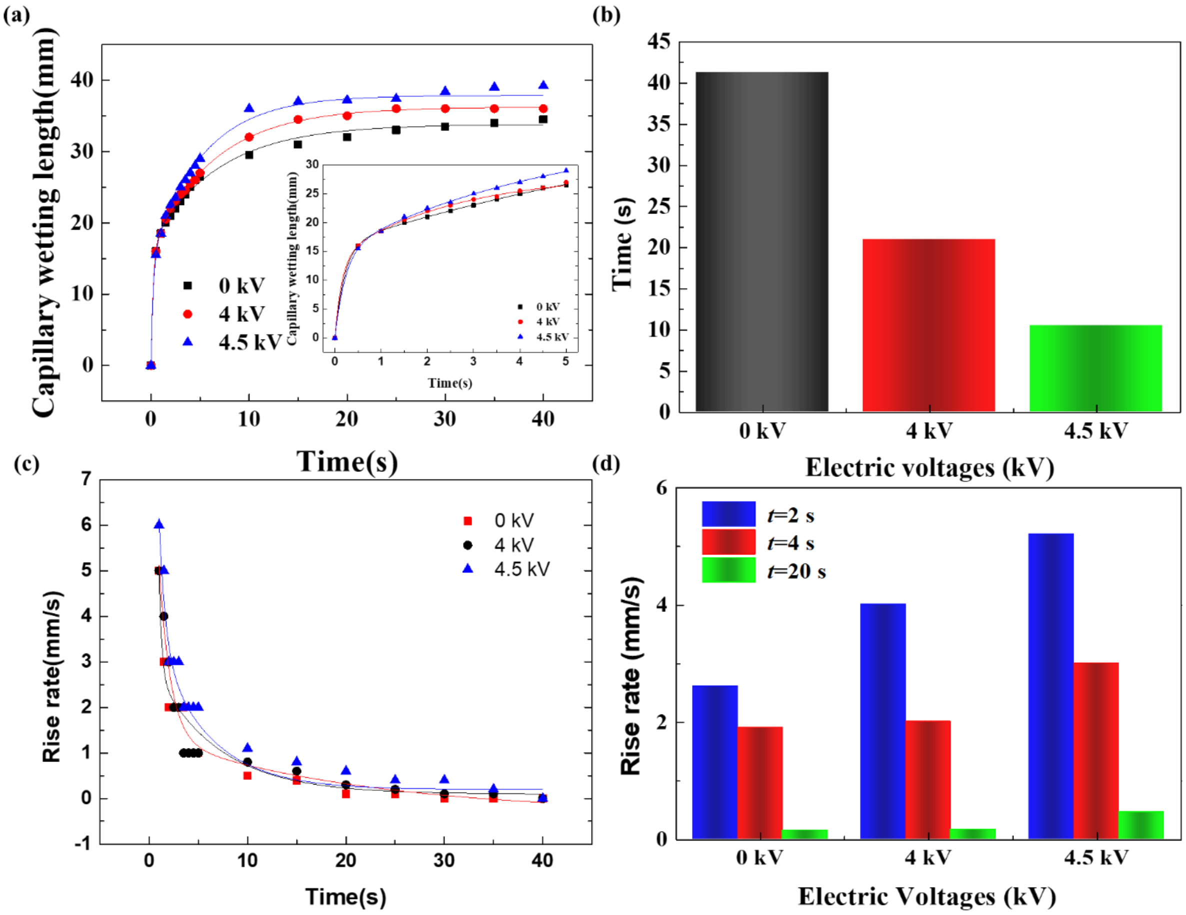

Fig. 7 Dynamic wicking characteristics under electric fields of 0 kV, 4kV and 4.5 kV: (a) variations of capillary wetting length over time, (b) the time needed to reach the capillary wetting length of 36mm under different electric voltages, (c) the rise rates at different electric voltages over time, (d) the rise rates at different period intervals with electric voltages.

voltages (0 kV, 4 kV, and 4.5 kV) are shown in Fig. 7(b). Results show that the application of an electric field increases the wetting length in microgrooves, and the stronger the electric field, the longer the capillary wetting length of liquid at the same time. This is because the electric field drives the liquid to flow upward along the microgrooves. Fig. 7(c) shows the rising rate at different electric voltages over time. The rising rate of liquid decreases exponentially with time, reaching the highest at the initial stage within 5s and dramatically declining, and basically leveling off after the 20s. In order to clearly see the comparisons between rise rate and time at different electric voltages, 3-period intervals were selected (t = 2s, 4s, the 20s) as shown in Fig. 7(d). We can find that at t = 2s, with the increase of electric field intensity, the rising rate of liquid in microgrooves increases higher, while t = 20s of the long-time stage, the rising rate is not obvious with the increase of the electric field, which is due to the gradual decreasing curvature of the liquid film along the axial direction of microgrooves based on Eq. (5), $E_l = \frac{V}{d_e}\left[\left(1-\frac{e(r_c)}{d_e}\right)\frac{\varepsilon_l}{\varepsilon_v}+\frac{e(r_c)}{d_e}\right]^{-1}$.[44] It decreases with the decreasing contact angle θ and the curvature of liquid film $r_c(z)$, thus leading the electric field intensity E (Eq. (5)) in the liquid to decrease along the axial direction of RMs. However, for the later period of the rise-of-rate process (t = 20s), the electric field did not improve the rising rate obviously due to the little varying radius of curvature.

In order to understand the rate-of-rise process of the capillary pumping mechanism under EHD effects, here, some classical equations of dynamic wicking characteristics are introduced to describe the fluid flow characteristics in capillary tubes. Washburn *et al.*[31,32] put forward the Lucas-Washburn equation as early as 1921, which is expressed as:

$$h^2 = \frac{r_c(z)\sigma\cos\theta}{2\mu}t \qquad (22)$$

That is to say, capillary flow follows the rule that the square of wetting length is linear with time. However, after verification by later scholars, it was found that this formula was only in the initial stage of capillary climbing when the gravity factor could be ignored.[7] Actually, with the increase of time, the gravity term became non-negligible, and this Eq. (22) lost its guiding value in real situations. Deng *et al.*[7] proposed the correlation as $h(t)\sim ke^{-\frac{t}{\tau}}$ with considering the gravity term that the wetting length h was related to the power of time t, and it was fitted by experiments data.

In this section, we will also investigate the dynamic wicking characteristics with considering the action of electric field, and obtain the empirical correlations according to the

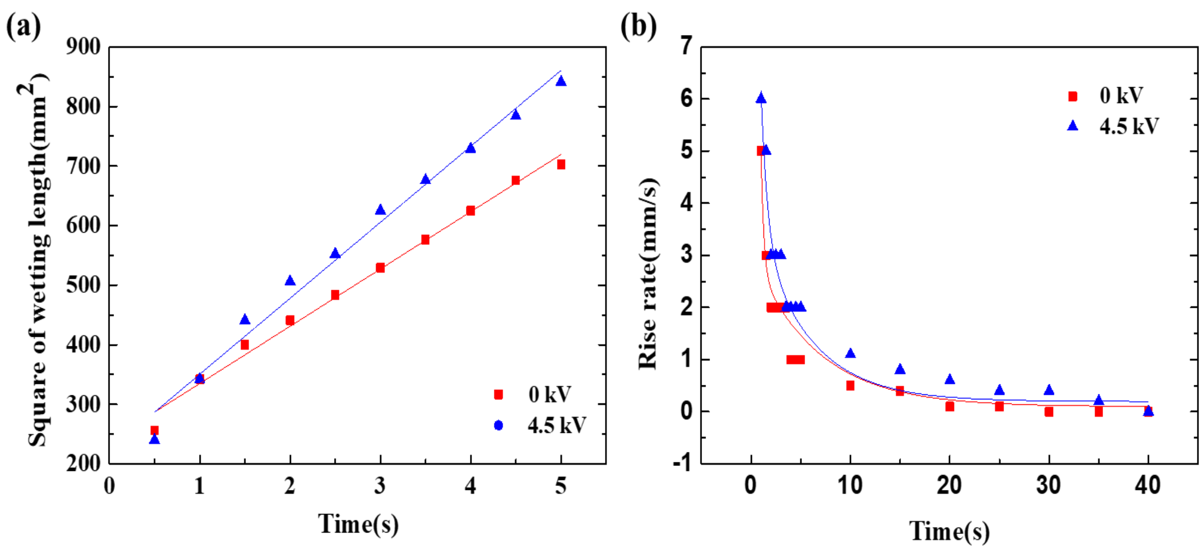

Fig. 8 Dynamic wicking characteristics of the capillary flow in the presence of the electric field (4.5 kV) and in the absence of the electric field (0 kV): (a) $h^2 \sim t$ curve at the initial stage (0~5s); (b) $\frac{h}{t} \sim ke^{-\frac{t}{\tau}}$ curve at the long-term stage (0~40s).

fitting experimental data. Fig. 8 shows the $h^2 \sim t$ curve at the initial stage (Fig. 8(a)) and $\frac{h}{t} \sim ke^{-\frac{t}{\tau}}$ curve at the long-term stage (0~40s) (Fig. 8(b)) of the capillary rate-of-rise flow in the presence of the electric field (4.5 kV) and in the absence of the electric field (0 kV). Furthermore, the following Table 4 and Table 5 list the detailed parameters of fitting correlation. Little error is calculated between fitting line data and experimental data, which also verifies that the experimental data agree well with the theoretical model at such two stages. We can see that the initial stage and the long-term stage more or less have the same trend regardless of the electric field. It is seen that at the initial stage of rising flow, the square of wetting length in microgrooves (h^2) is linear with time (t) without considering the influence of inertia and gravity according to Eq. (22) within 0~5 s.[6] In the initial stage, the rising rate of liquid in the RMs decreases exponentially with time, while in the long-term stage, the flow rate tends to be stable until it reaches a steady state.

Regarding the EHD pumping mechanism, as the applied electric field intensifies, the Coulomb force in the liquid is activated. Coulomb force, as one of the EHD pumping mechanisms, can be incorporated as conduction pumping, induction pumping, and ion pumping.[45] For conduction, the current is generated from the positive and negative ions generated by molecular dissociation used to neutralize the electrode. Because there is no injected charge on the electrode, the positive and negative ions generated by dissociation are attracted to the electrode with the opposite polarity, forming a charge layer with a polarity different from that of the adjacent electrode, which is also called “heterocharge layers”.[46] Therefore, an electric force is generated on the electrodes, and then the Coulomb force generated on the positive and negative electrodes can be asymmetric through the electrodes with specific shapes, so as to avoid mutual cancellation. Under such a difference, the Coulomb force can realize the driving effect on the fluid. For a neutral species of our working fluid, H_2O,

Table 4. Fitting correlation form $h^2 \sim t$ as shown in Fig. (8a) for dynamic wicking characteristics of the capillary flow in the presence of the electric field (4.5 kV) and in the absence of the electric field (0 kV) at the initial stage (0~5s).

Fitting Correlation Form	$h^2 = a + b * t$		
	0 kV	4.5 kV	$h^2 \sim f(t)$ (fitting correlation)
Intercept (a)	238.9	223	$h^2 = 238.9+96.1t$
Slope (b)	96.1	127.5	$h^2 = 223+127.5t$
Pearson’s R (correlation coefficient)	0.99546	0.99286	

Table 5. Fitting correlation form $\frac{h}{t} \sim ke^{-\frac{t}{\tau}}$ as shown in Fig. (8b) for dynamic wicking characteristics of the capillary flow in the presence of the electric field (4.5 kV) and in the absence of the electric field (0 kV) at the long-term stage (0~40s).

Fitting Correlation Form	$\frac{h}{t} = y_0 + A_1 e^{-\frac{t}{t_1}} + A_2 e^{-\frac{t}{t_2}}$						
	y_0	A_1	t_1	A_2	t_2	Adj. R-Square	Mean Square of Residual
0 kV	0.0961	2.9794	6.4153	77.4447	0.2867	0.9617	0.0700
4.5 kV	0.1973	3.7495	5.2249	13.3420	0.6513	0.9407	0.1863

the space charge is generated by the molecular dissociation caused by the electric field and is adsorbed on the electrode with the opposite polarity. Its positive and negative ions, H^+ and O^{2-}, there is a reversible process of dissociation and recombination.[45,46]

$$H_2O \leftrightarrow 2H^+ + O^{2-} \tag{23}$$

Another electrical force, dielectrophoresis (DEP), is also found to be effective to control the liquid flow. When an electric field is applied, the positive charge inside the particle moves along the electric field direction, while the negative charge moves along the opposite direction of the electric field direction. Thus, a reverse electric field is formed inside the particle, which generates an induced dipole moment,[47] which is called the polarization phenomenon. If the applied electric field is uneven, the induced dipole moment will interact with the electric field to form a dielectrophoretic force, which makes the particles move to the stronger or weaker side of the electric field. Therefore, an electric coulomb force and DEP are generated between the planar electrodes pair, and then the Coulomb force generated on the positive and negative electrodes can be asymmetric through the electrodes with specific shapes, so as to avoid mutual cancellation. Under such a difference, the Coulomb force can realize the driving effect on the fluid. While for the DEP, when the polarizability of the ions is greater than that of the suspended medium, the ions will be attracted to the high electric field and tend to move in the direction of high electric field intensity. Consequently, the physical mechanism contributing to improving the capillary wetting length and the rate-of-rise process under an electric field is probably because the ions of liquid moving towards the high potential and electric field intensity direction driven by the coulomb force and DEP as shown in Fig. 9, the electric field intensity at the top of the vapor region contacting with the negative electrode is much larger than that in the liquid region, and the dielectric fluid tends to flow to the region with higher electric field intensity driven by the electric field force. Therefore, this is also the reason that the lower plate is used as the positive electrode, while the upper electrode is the ground electrode in this experiment as shown in Fig.1 and Fig. 2. Therefore, the mechanism of the wicking enhancement under EHD effects results from the dynamic disequilibrium between the dissociation rate and recombination rate of working fluid under high electric field.

4.3 EHD effects on the evaporating heat transfer performance

In order to analyze the temperature variation caused by the electric field intuitively, this study defines the temperature difference ΔT between the average surface temperature of microgrooves in the presence and in the absence of an electric field. As shown in Fig. 10, with the increase of heat flux, temperature differences ΔT gradually increase, which indicates that the electric field has a more significant effect on the heat transfer of microgrooves under the input high heat flux. It is noted to see that the maximum temperature drop is about 30 °C when the heat flux is 13.5 kW m^{-2} under the action of 6 kV electric voltage.

Here in this paper, a dimensionless temperature (T*) is introduced to scale the temperature variation from 0 to 1 because of different initial temperatures under the electric field in the experimental application. It quantifies the temperature-changing rate under the electric field. T* is expressed as:

$$T^* = \frac{T(t)-T(t_0)}{T(t_t)-T(t_0)} \tag{24}$$

where T is the temperature of microgrooves, t_t is the temperature at a certain time, t_0 is the initial time.

Fig. 11 illustrates the effects of the electric field on the temperature distribution of the microgrooves under interelectrode spacing of 48 mm (Fig. 11) during experiment applications. It can be shown that the temperature increases with time variation. However, the growth range decreases along with the increase in electric field intensity. As illustrated in Fig. 11(a), the growth range is 7.8 ºC in the absence of an electric field, and 9.2 ºC, 12 ºC, and 11.5 ºC in the presence of the electric field of 0.5 kV, 1.5 kV and 2 kV. While the scaled temperature changing rate in Fig. 11(b) also shows the gentlest variation of 0 kV and the highest variation slope of 2 kV compared with that under EHD effects. Therefore, it can be concluded that the EHD effects can decrease the wall temperature of the microgrooves, which is mainly due to the increasing wetting length, and the corresponding enhancing convection heat transfer in the presence of the electric field.

4.4 EHD effects on the economic efficiency

In order to quantify the gains brought by EHD effects in enhancing wicking characteristics and heat transfer performance in microgrooves structure, it is necessary to discuss the economic efficiency, namely the proportion of joule heat consumed by EHD in enhancing effects. Fig. 12 (a) depicts the current-voltage characteristics under different applied electric voltages. It is seen that when the electric voltage increases to 5.5 kV, the current is thus generated in the fluid. At this time, the fluid in the microgrooves is driven by the electric field action to flow upwards, and the capillary wetting length increases during the experiments. Such current-voltage characteristic also explains the reason that the electric field has a polarization effect on the particles in the fluid introduced in section 4.2. Ions are absorbed into the fluid and flow directionally under the electric field action to form current,[12,45] which in turn drives the fluid in the microgrooves to flow, thus increasing the wetting length. When the electric voltage reaches over 7 kV, the fluid in microgrooves contacts the grounding electrode due to the limitation of the electrode arrangement in this experiment. It is observed that the corona wind generated by the grounding electrode inhibits the fluid flow during the experiments, resulting in a decrease in capillary wetting length.

The benefits brought by the electric field are taken into account here. An economic factor ε is defined in this study to study the ratio of heat taken away by EHD effects q_j to

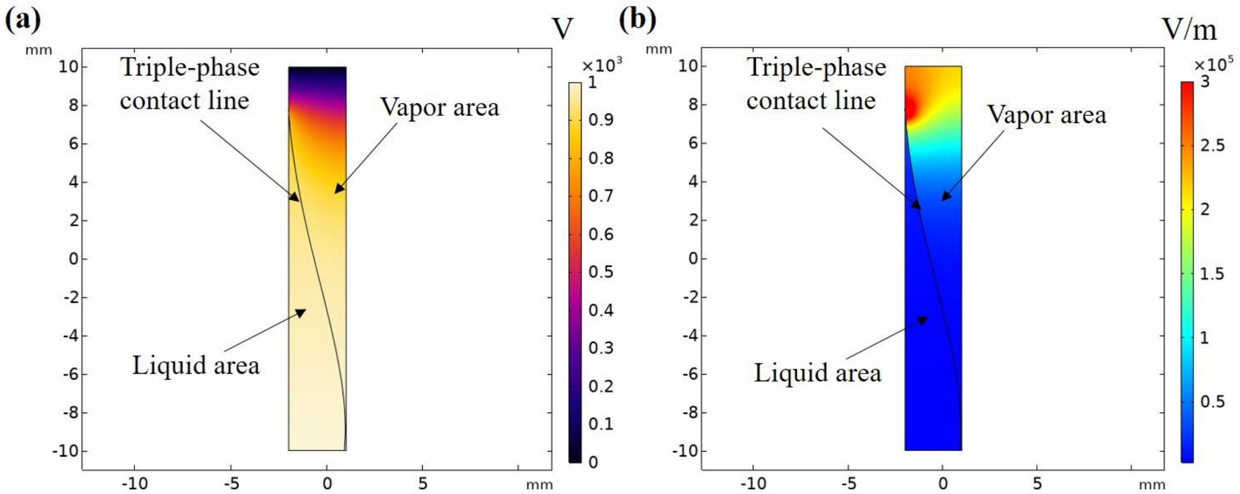

Fig. 9 The electric field distribution for the vapor-liquid in the open microgrooves (a) potential and electric field distribution, (b) electric field intensity distribution.

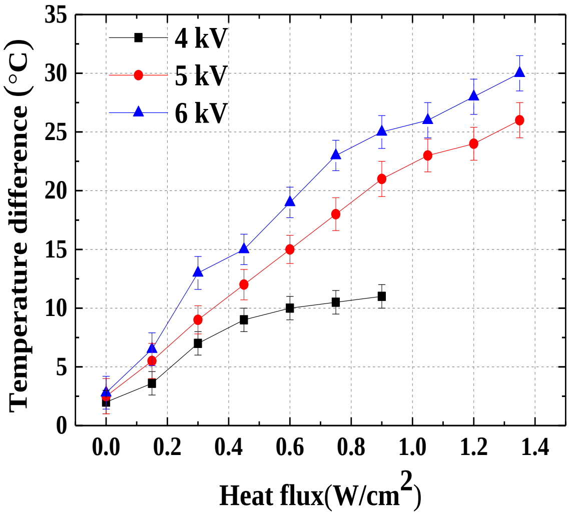

Fig. 10 EHD effects on the temperature variations of the microgrooves under different applied electric voltages (4 kV, 5 kV and 6 kV).

the power consumption P_e expressed in Eq. (25).

$$\varepsilon = \frac{q_j}{P_e} \tag{25}$$

When the economic factor is greater than 1, it is considered to be economical to introduce an electric field to enhance liquid capillary wetting performance and heat transfer characteristics in the microgrooves. Fig. 12(b) shows the variations of the economic factor of microgrooves No.4 with applied electric voltage. It is found that the exists highest benefit when the electric voltage increases to 5 kV. While it increases to 5 kV or even higher, the benefit factor weakens because the increasing rate of electric power consumption is greater than that of capillary wetting and heat transfer enhancement. It results from the dynamic equilibrium of dissociation and recombination rate of working fluid H_2O at lower electric voltage, while, when the electric voltage exceeds a certain threshold value, the rate of dissociation begins to exceed the rate of recombination discussed in section 4.2.[12,48] It is calculated that the economic factor is 11.5 when an electric voltage of 5 kV and the power consumption of 0.048 W is applied, which has a considerable effect in total.

In conclusion, in this section, not only the experimental system of energy efficient utilization is proposed experimentally, but also the mechanism of energy efficiency improvement is analyzed theoretically, and the evaluation factors of wicking performance under EHD effects are characterized in detail, which is supplied as follows:

(1) The maximum axial capillary wetting length under EHD effects at steady state is experimentally conducted and theoretically analyzed, and the predicted results agree well with the experimental data, with the maximum error is 9.2% at the voltage of 5.7 kV. The wetting length decreases with the increased inclined angle, and the electric field enhances at a greater extent at the smaller heat flux. There exist an optimal strengthening voltage, which corresponds to the maximum wetting length that can be achieved in the microgrooves.

(2) The microgrooves under a larger electric field exhibit much quicker capillary rise characteristics than that under a less electric field or without it during the rate-of-rise experiments. The dynamic wicking characteristics considering the action of the electric field are investigated at the transient state, and obtained the empirical correlations according to the fitting experimental data as $h^2 \sim t$ curve at the initial stage, and $\frac{h}{t} \sim ke^{-\frac{t}{\tau}}$ curve at the long-term stage, which has a similar trend as no electric field.

(3) Two planar electrodes are used to generate the electric field. EHD pumping mechanism has been analyzed. The mechanism of the wicking enhancement under EHD effects results from the dynamic disequilibrium between the dissociation rate and recombination rate of working fluid under high electric field.

(4) EHD effects can decrease the wall temperature of the microgrooves, and the scaled temperature changing rate shows the gentlest variation of 0 kV and highest variation slope of 2

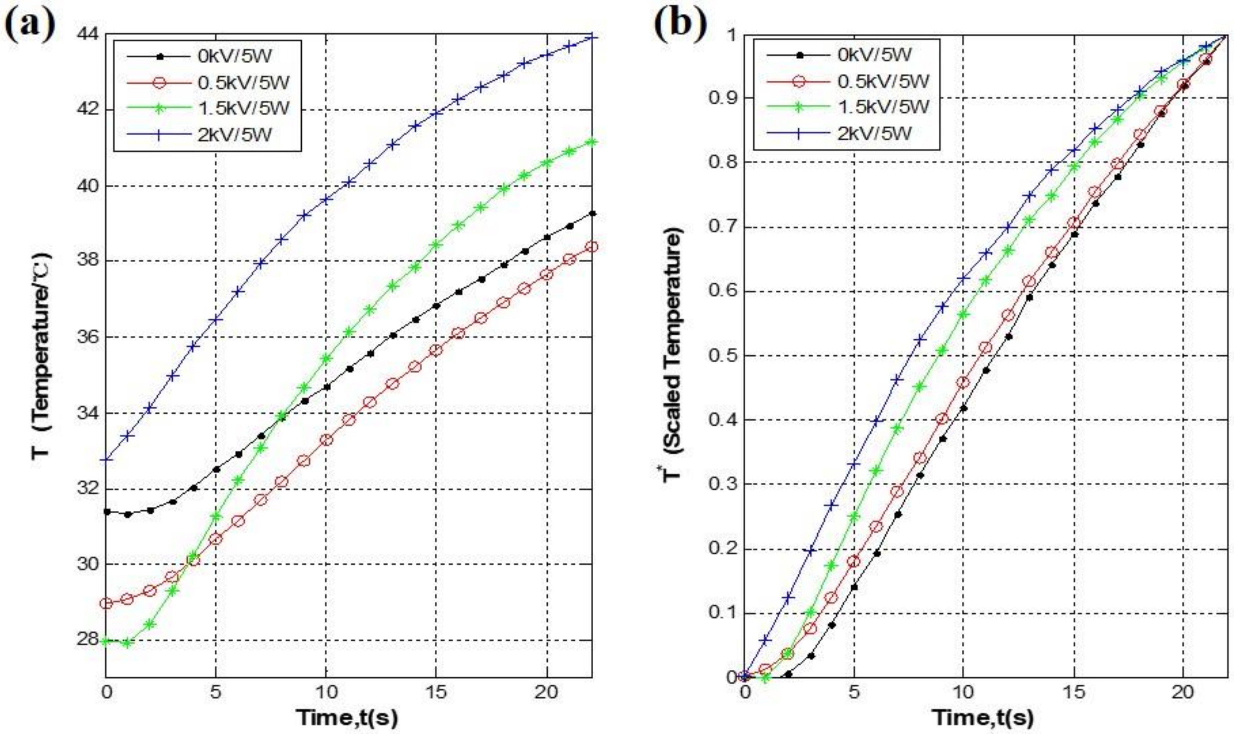

Fig. 11 Effects of electric field on the temperature distribution of the microgrooves at 48 mm interelectrode spacing during experiment applications: (a) the real temperature distribution for different initial temperatures, (b) the scaled temperature changing rate.

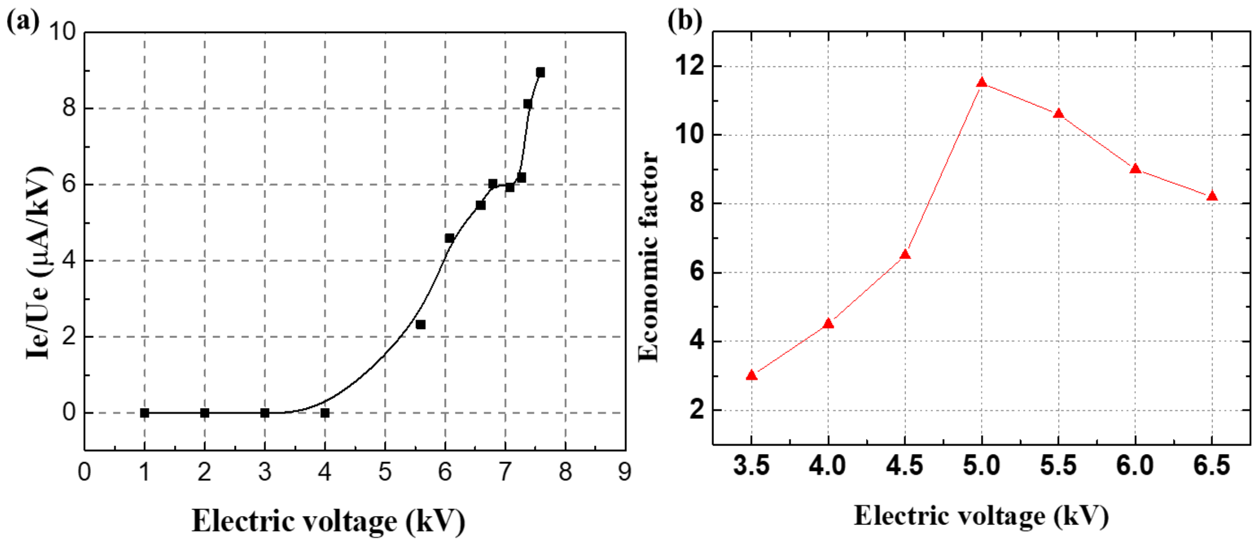

Fig. 12 EHD effects on the economic efficiency: (a) current-voltage characteristics under different applied electric voltages, (b) variations of an economic factor with applied electric voltage.

kV compared with that under EHD effects.

(5) The EHD effects on the economic efficiency is also considered in this study. The exist a highest benefit at the electric voltage of 5 kV during the experimental conditions.

5. Conclusions

In summary, this work investigated the characterization of capillary performance of rectangular microgrooves under EHD effects in a two-phase heat transfer device, the wicking performance of rectangular microgrooves is characterized and evaluated by axial maximum capillary wetting length at steady state and dynamic rise rate at transient state during rate-of-rise experiments. The steady state model of maximum capillary wetting length is achieved and verified by experimental data, with the maximum error is 9.2% at the voltage of 5.7 kV. While, the transient state model is obtained through the fitting experimental data as $h^2 \sim t$ curve at the initial stage, and $\frac{h}{t} \sim ke^{-\frac{t}{\tau}}$ curve at the long-term stage, which can be generalized predicted at different stages by the interested engineers. The mechanism of the wicking enhancement under EHD effects results from the dynamic disequilibrium between the dissociation rate and recombination rate of working fluid under high electric field. In addition, there exist a highest benefit of economic efficiency at the electric voltage of 5 kV during the experimental conditions. This paper could be of guiding importance when interested engineers design the thermal management devices of power electronics, and some infrared cloaking systems.

Acknowledgments

This work was supported by the Basic Science Center Program for Ordered Energy Conversion of the National Natural Science Foundation of China (No. 51888103), the National Natural Science Foundation of China (No. 51806218), and the CAS Pioneer Hundred Talents Program. The authors would also like to thank Ms Yingying Yu for her assistance in the EHD experiments.

Conflict of interest

There are no conflicts to declare.

Supporting information

Not Applicable.

References

[1] H. Tang, Y. Tang, Z. Wan, J. Li, W. Yuan, L. Lu, Y. Li, K. Tang, *Applied Energy*, 2018, **223**, 383-400, doi: 10.1016/j.apenergy.2018.04.072.

[2] J. M. Pfotenhauer, *ES Energy & Environment*, 2019, **3**, 1-3, doi: 10.30919/esee8c215.

[3] C. Liu, M. Chen, W. Yu, Y. He, *ES Energy & Environment*, 2018, **2**, 31-42, doi: 10.30919/esee8c191.

[4] Y. Yu, X. Hu, J. Tang, W. Zhou, *Applied Thermal Engineering*, 2019, **162**, 114178, doi: 10.1016/j.applthermaleng.2019.114178.

[5] D. Deng, D. Liang, Y. Tang, J. Peng, X. Han, M. Pan, *Experimental Thermal and Fluid Science*, 2013, **50**, 1-9, doi: 10.1016/j.expthermflusci.2013.04.014.

[6] J. Tang, X. Hu, *Experimental Thermal and Fluid Science*, 2020, **112**, 109948, doi: 10.1016/j.expthermflusci.2019.109948.

[7] D. Deng, Y. Tang, J. Zeng, S. Yang, H. Shao, *International Journal of Heat and Mass Transfer*, 2014, **77**, 311-320, doi: 10.1016/j.ijheatmasstransfer.2014.05.003.

[8] C. Guo, D. Yu, T. Wang, Y. Jiang, D. Tang, *International Journal of Heat and Mass Transfer*, 2015, **84**, 1113-1118, doi: 10.1016/j.ijheatmasstransfer.2015.01.095.

[9] Y. H. Diao, L. Guo, Y. Liu, Y. H. Zhao, S. Wang, *International Journal of Heat and Mass Transfer*, 2014, **78**, 371-379, doi: 10.1016/j.ijheatmasstransfer.2014.07.004.

[10] R. Mandel, A. Shooshtari, M. Ohadi, *Numerical Heat Transfer, Part A: Applications*, 2017, **71**, 111-127, doi: 10.1080/10407782.2016.1257300.

[11] X. Hu, Z. Yan, S. Guo, Y. Cheng, J. Gong, *Chinese Science Bulletin*, 2011, 56, 417-423, doi: 10.1007/s11434-010-4306-x.

[12] J. Tang, X. Hu, Y. Yu, *Experimental Thermal and Fluid Science*, 2020, **150**, 106222, doi: 10.1016/j.ijthermalsci.2019.106222.

[13] J. Tang, Y. Yu, X. Hu, *International Heat Transfer Conference Digital Library*, Begel House Inc., 2018, doi: 10.1615/IHTC16.hte.022487.

[14] Z. Yu, K. Hallinani, W. Bhagat, R. Kashani, *Journal of Thermophysics and Heat Transfer*, 2002, **16**, 180-186, doi: 10.2514/2.6682.

[15] C. P. Migliaccio, S. V. Garimella, *International Journal of Heat and Mass Transfer*, 2013, **57**, 73-81, doi: 10.1016/j.ijheatmasstransfer.2012.10.009.

[16] V. Bahadur, S. V. Garimella, *Microelectronics Journal,* 2008, **39**, 957-965, doi: 10.1016/j.mejo.2007.11.010.

[17] F. W. Holm, S. P. Goplen, *Journal of Heat Transfer*, 1979, **101**, 543-547, doi: 10.1115/1.3451025.

[18] I. Catton, G. R. Stroes, *Journal of Heat Transfer*, 2002, **124**, 162-168, doi: 10.1115/1.1404119.

[19] Y. J. Youn, C. K. Lee, N. Shikazono, H. W. Kang, *International Journal of Multiphase Flow*, 2021, **134**, 103470, doi: 10.1016/j.ijmultiphaseflow.2020.103470.

[20] C. Li, G. P. Peterson, Y. Wang, *Journal of Heat Transfer*, 2006, **128**, 1312-1319, doi: 10.1115/1.2349507.

[21] X. Hu, D. Tang, *International Journal of Thermal Sciences*, 2007, **46**, 1163–1171, doi: 10.1016/j.ijthermalsci.2007.04.002.

[22] Y. Tang, H. Tang, J. Li, S. Zhang, B. Zhuang, Y. Sun, *Applied Thermal Engineering*, 2017, **115**, 1020-1030, doi: 10.1016/j.applthermaleng.2016.12.056.

[23] H. Tang, Y. Tang, W. Yuan, R. Peng, L. Lu, Z. Wan, *Applied Thermal Engineering*, 2018, **129**, 907-915, doi: 10.1016/j.applthermaleng.2017.10.091.

[24] H. Wang, S. V. Garimella, J. Y. Murthy, *International Journal of Heat and Mass Transfer*, 2007, **50**, 3933-3942, doi: 10.1016/j.ijheatmasstransfer.2007.01.052.

[25] M. Gao, X. Quan, P. Cheng, *International Communications in Heat and Mass Transfer*, 2014, **56**, 159-164, doi: 10.1016/j.icheatmasstransfer.2014.06.011.

[26] R. Fu, X. Hu, Y. Yan, W. Zhou, H. Wu, J. Wang, J. Tang, *International Journal of Heat and Mass Transfer*, 2019, **144**, 118674, doi: 10.1016/j.ijheatmasstransfer.2019.118674.

[27] J. Tang, Y. Yu, X. Hu, X. Mo, W. Zhou, X. Dai, L. Shan, D. Yu, *Applied Thermal Engineering*, 2018, **143**, 90-99, doi: 10.1016/j.applthermaleng.2018.07.041.

[28] F. L. Chang, Y. M. Hung, *International Journal of Heat and Mass Transfer*, 2017, **108**, 257-270, doi: 10.1016/j.ijheatmasstransfer.2016.12.018.

[29] S. J. Parulekar, *Chemical Engineering Education*, 1988, **22**, 62-66.

[30] R. J. Moffat, *Experimental Thermal and Fluid Science*, 1988, **1**, 3-17, doi: 10.1016/0894-1777(88)90043-x.

[31] E. W. Washburn, *Physical Review*, 1921, **17**, 273-283, doi: 10.1103/physrev.17.273.

[32] R. Lucas, *Kolloid-Zeitschrift*, 1918, **23**, 15-22, doi: 10.1007/bf01461107.

[33] Y. Tang, D. Deng, G. Huang, Z. Wan, L. Lu, *Energy Conversion and Management*, 2013, **66**, 66–76, doi: 10.1016/j.enconman.2012.09.027.
[34] N. Fries, M. Dreyer, *Journal of Colloid and Interface Science*, 2008, **320**, 259-263, doi: 10.1016/j.jcis.2008.01.009.
[35] J. A. Stratton, Electromagnetic theory, *New York: John Wiley & Sons*, 2007.
[36] I. Saad, S. Maalej, M. C. Zaghdoudi, *Journal of Electrostatics*, 2017, **85**, 61-78, doi: 10.1016/j.elstat.2016.12.004.
[37] I. Saad, S. Maalej, M. C. Zaghdoudi, *International Journal of Heat and Mass Transfer*, 2017, **107**, 244-263, doi: 10.1016/j.ijheatmasstransfer.2016.10.089.
[38] D. Yu, C. Guo, N. Xie, T. Wang, X. Hu, D. Tang, *Applied Thermal Engineering*, 2016, **106**, 906-915, doi: 10.1016/j.applthermaleng.2016.05.188.
[39] R. R. Rye, J. A. Mann, F. G. Yost, *Langmuir*, 1996, **12**, 555-565, doi: 10.1021/la9500989.
[40] A. Bejan,G. Tsatsaronis, M. J. Moran, Thermal design and optimization, *John Wiley & Sons*, 1995.
[41] R. H. Nilson, S.W. Tchikanda, S.K. Griffiths, M.J. Martinez, *International Journal of Heat and Mass Transfer*, 2006, **49**, 1603–1618, doi: 10.1016/j.ijheatmasstransfer.2005.11.002.
[42] D. Yu, X. Hu, C. Guo, N. Xie, D. Tang, *Applied Thermal Engineering*, 2015, **80**, 424-435, doi: 10.1016/j.applthermaleng.2014.12.076.
[43] Z. Meng, Q. L. Hou, *Chinese Journal of Geophysics*, 2013, 56, 667-675, doi: 10.6038/cjg20130231.
[44] D. Yu, X. Hu, C. Guo, T. Wang, X. Xu, D. Tang, X. Nie, L. Hu, F. Gao, T. Zhao, *Applied Thermal Engineering*, 2013, **61**, 716-727, doi: 10.1016/j.applthermaleng.2013.08.042
[45] J. Seyed-Yagoobi, *Journal of Electrostatics*, 2005, **63**, 861-869, doi: 10.1016/j.elstat.2005.03.047.
[46] Y. Feng, J. Seyed-Yagoobi, *Physics of Fluids*, 2004, **16**, 2432-2441, doi: 10.1063/1.1739782
[47] R. Derakhshan, A. Ramiar, A. Ghasemi, *Journal of Molecular Liquids*, 2020, **310**, 113211, doi: 10.1016/j.molliq.2020.113211.
[48] B.-B. Wang, X.-D. Wang, Y.-Y. Duan, M. Chen, *International Journal of Heat and Mass Transfer*, 2014, **73**, 533-541, doi: 10.1016/j.ijheatmasstransfer.2014.02.034.

Author Information

Jinchen Tang *is an associate professor in Institute of Engineering Thermophysics, Chinese Academy of Sciences, China. Her research focuses on micro/nano-scale flow and heat transfer, high-heat-flux thermal management of electronic equipment. She received her PhD degree from Hunan University and as a joint-PhD student in Johns Hopkins University, and elected as JSPS scholar in Tokyo University.*

Zhe Chen *is an assistant professor at the Institute of Engineering Thermophysics, Chinese Academy of Sciences, China. His research focuses on micro-scale heat transfer and thermal interface materials.*

Yu Ma *is an assistant professor at the Institute of Engineering Thermophysics, Chinese Academy of Sciences, China. His research focuses on metal matrix composites, nano-scale interfacial heat transfer and thermal functional materials. He received his PhD degree in Chemistry from Université Paris-Saclay.*

Hang Zhang *is a professor in Institute of Engineering Thermophysics, Chinese Academy of Sciences and University of Chinese Academy of Sciences, in China. His research focuses on mechanisms and advanced technology on energy transport and conversions in emerging materials and equipment. He received his PhD degree in Physics from University of California, Riverside and then joined Caltech as a postdoctoral scholar.*

Publisher's Note: Engineered Science Publisher remains neutral with regard to jurisdictional claims in published maps and institutional affiliations.